Journal of Magnetic Resonance 283 (2017) 79–88

Contents lists available at ScienceDirect

Journal of Magnetic Resonance

journal homepage: www.elsevier.com/locate/jmr

Complementary analyses of hollow cylindrical unioriented permanent magnet (HCM) with high permeability external layer

Carlos M.S. Lobo [a], Giancarlo Tosin [b], Johann E. Baader [c], Luiz A. Colnago [d,*]

[a] Instituto de Química de São Carlos, Universidade de São Paulo, Avenida Trabalhador São Carlense 400, 13566-590 São Carlos, São Paulo, Brazil
[b] LMA Magnet Consultancy, Rua Filomeno Rispoli 509, 13564-200 São Carlos, São Paulo, Brazil
[c] Faculdade de Engenharia Elétrica e de Computação, Universidade Estadual de Campinas - Departamento de Sistemas e Energia, Avenida Albert Einstein 400, 13083-852 Campinas, São Paulo, Brazil
[d] Embrapa Instrumentação, Rua XV de Novembro 1452, 13560-970 São Carlos, São Paulo, Brazil

ARTICLE INFO

Article history:
Received 27 March 2017
Revised 22 June 2017
Accepted 29 August 2017
Available online 1 September 2017

Keywords:
Permanent magnet
Dipolar homogeneous field
Hollow cylindrical magnet

ABSTRACT

In this article, several studies based on analytical expressions and computational simulations on Hollow Cylindrical Magnets with an external soft ferromagnetic material (HCM magnets) are presented. Electromagnetic configurations, as well as permanent-magnet-based structures, are studied in terms of magnetic field strength and homogeneity. Permanent-magnet-based structures are further analyzed in terms of the anisotropy of the magnetic permeability. It was found that the HCM magnets produce a highly homogeneous magnetic field as long as the magnetic material is isotropic. The dependency of the magnetic field strength and homogeneity in terms of the anisotropy of the magnetic permeability is also explored here. These magnets can potentially be used in medium-resolution NMR spectrometers and high-field NMR spectrometers.

1. Introduction

Permanent magnets were popular in NMR spectroscopy until the late 1970s. Since then, superconducting magnets have become the standard NMR magnet [1]. However, in the last decade there has been a revival of the use of permanent magnets in NMR [2,3]. This revival was due to the introduction of new magnetic materials, such as rare-earth magnets and the configuration proposed by Halbach [1]. The main advantage of Halbach's arrays made with rare-earth materials was the significant reduction of the volume and mass of the magnets, in comparison to H and C-shaped magnets (see Fig. 1) [1,3]. Today, several manufacturers offer, in addition to low resolution spectrometers, medium resolution benchtop NMR spectrometers at 1.4 T (60 MHz) based on Halbach configuration [4–6]. These benchtop spectrometers are not as expensive, bulky, heavy and sensitive instruments as the high field NMR spectrometers, which are often placed in central analytical facilities. They can be used for quality control at-line or on-line in the industry, in laboratory benches or hoods to monitor chemical reactions *ex situ* or *in situ* among many other applications [1–3].

Nonetheless, the homogeneity of the magnetic field produced by the cylindrical Halbach array is limited by the number of pieces used, and tends to be better the more pieces are used [7]. This, in turn, creates a problem, as the individual magnets are never equal in magnetization strength and orientation, due to the manufacturing process itself. It is not so easy to repeat the same remanent field within 1% and the same magnetization orientation within 1°. Even the magnetization uniformity in the same piece has its constraints, which may increase depending on the shape of the pieces.

In terms of mechanical concerns, the profiles of the pieces, most commonly of the polar pieces, are assured in few tenths of micrometers, which can make the field specification not reachable. Also parallelism and the orthogonality have their restrictions in the assemblies. The assemblies always happen in an environment of strong magnetic forces, demanding many mechanical artifices for precise placement and orientation of the magnetic pieces.

Aside from the homogeneity of the magnetic field, there are several reasons for which this configuration is used [8]:

- Halbach arrays have the highest ratio of magnetic field intensity per magnet mass, which in the ideal case is perfectly homogeneous. The theoretical limit of the magnetic field intensity of the Halbach model is infinity, as will be shown next.
- The magnetic field generated is perpendicular to the longitudinal axis of the cylinder. This permits the use of simple solenoidal radio frequency-coils for NMR sample excitation.

* Corresponding author.
E-mail address: luiz.colnago@embrapa.br (L.A. Colnago).

http://dx.doi.org/10.1016/j.jmr.2017.08.013
1090-7807/

- The magnet has no need for yokes. This simplifies its design and optimization, since no saturation effects have to be taken into account.

However, the main disadvantage of the Halbach array is that many pieces of permanent magnets, which can have different magnetization orientations, are required in order to obtain a magnetic field with a high intensity and homogeneity. This poses some challenges in the assembly of the magnet, as repulsion and attraction forces between the pieces must be countered by building a strong and complex structure able to maintain the magnets in their fixed positions and orientations. Furthermore, even if all magnets undergo the same magnetization process they may end up with different remanent fields, which affects the quality of the Halbach array. This means that more magnets than are actually necessary must ordered and sorting procedures are required prior to assembly.

Hollow cylinders of permanent magnet (PM), magnetized in a direction perpendicular to its longitudinal axis, surrounded by a ferromagnetic material of high magnetic permeability (HCM), Fig. 2, has been little explored. Although this geometry is very simple and creates a perfectly homogeneous field, the first analytical study was published only in 2003 [9]. For such configuration, procedures proposing how to change the field profile and its intensity (tunable field) in the central air gap region [10] and one patent in NMR area [11] were published as well, however, the present literature on the subject deals with magnetically isotropic materials and magnetic permeability equal to one, something which may not always be the case when ordering magnets from a manufacturer.

The main advantage of the HCM model, when compared to the Halbach array, is the fact that it consists of a single cylinder of magnetic material, one which is uniformly magnetized in a direction perpendicular to its longitudinal axis, and a soft ferromagnetic external cylinder, without which the magnetic flux is zero in the air gap [9], such as carbon steel. Assembly of this type of magnet is easier than the Halbach as there are less pieces to deal with, making the final product less prone to mechanical errors.

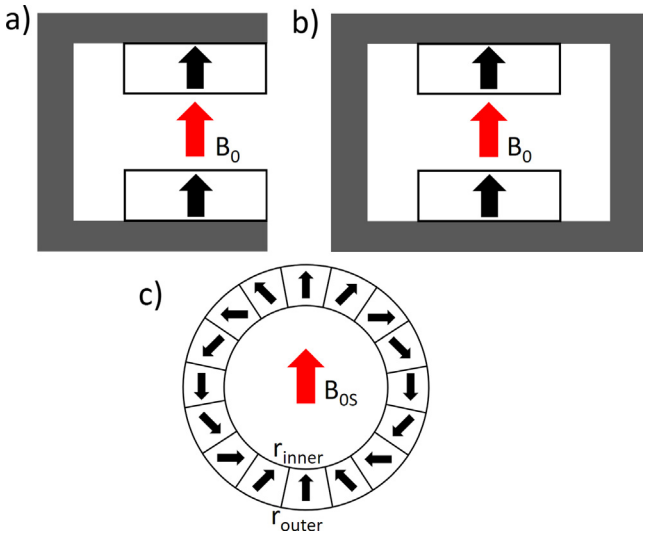

Fig. 1. Configurations of dipoles made with permanent magnets: (a) C-shape, (b) H-shape and (c) Halbach array. The magnetization orientations of the permanent magnets and the resulting magnetic field (B_0) are indicated by black and red arrows, respectively. B_{0S} is the magnetic field generated in the Halbach array due to its segmentation. (For interpretation of the references to colour in this figure legend, the reader is referred to the web version of this article.)

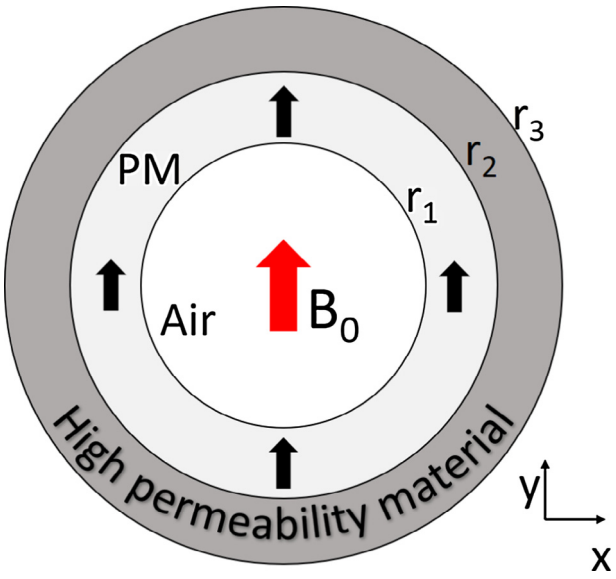

Fig. 2. Hollow cylinder of permanent magnet (r_1 to r_2) surrounded by a ferromagnetic material (r_2 to r_3) of high permeability (HCM). The black arrows indicate the magnetization orientation of the permanent magnet. B_0 is the resulting magnetic field.

Another advantage of the HCM model is that it may be cheaper to build than a Halbach array, due to the lower number of pieces needed and the number of pieces that must be ordered. Since the price of a magnet is mostly dependent on the volume of magnetic material ordered and not on its shape, the main price difference between the Halbach and HCM models would be associated with the assembly of the magnets, because Halbach magnets require much more control of the positioning and magnetization of the permanent magnets and small deviations in magnetization orientation or modulus of the pieces can lead to very inhomogeneous magnetic fields.

For NMR applications the HCM magnet could be especially useful as the highly homogeneous magnetic field which can be obtained may help improve the quality of medium-resolution spectra.

In this context, the primary aim of this study was to further explore and describe the HCM model through computational analysis, mainly by taking into account the effect of the magnetic permeability of the permanent magnet (PM), something which has not been previously done. Expressions for the field intensity and homogeneity are obtained from fittings over 2D simulation results. The magnetic field strength and homogeneity of the HCM model is compared to that of the more traditional Halbach array. A new electromagnetic cylindrical configuration, equivalent to the PM-based HCM, is introduced here and initial 2D analyses regarding its magnetic field intensity and homogeneity are performed.

2. Computational analysis

The 2D simulations were performed for numerical analyses using the free software FEMM (Finite Element Method Magnetics) [12] on which several scenarios were generated. In each scenario different dimensions of the permanent magnet and magnetic permeability were tested. The mesh dimensions were chosen in the following manner: the mesh in the internal air region of the magnet was set to 0.0025 mm, the mesh in the magnet itself was set to 0.1 mm, the mesh in the soft magnetic material (such as carbon steel) region was set to 0.8 mm and the mesh in the exterior air region was set to 5 mm. These meshes assured the convergence

of field values, not requiring thinner meshes. For our problem the ferromagnetic material and the PM were considered to be perfectly adjacent to each other (without an air gap) - Fig. 2 - and the thickness of the soft magnetic material was set to 50 mm. Furthermore, the relative magnetic permeability of the soft magnetic material was set to a very high value (10^{10}), allowing it to be considered as a perfect magnetic conductor ($\mu_r = \infty$). This permitted the use of the equation derived by Peng et al. [9] for the intensity of the magnetic field in the equations derived for the configuration with permanent magnets.

Different parameters were altered during each simulation. The inner radius, r_1, was maintained constant at 10 mm, but r_2 covered a range of values from 15 mm to 100 mm in steps of 5 mm, thus the ratio r_2/r_1 varied from 1.5 to 10. Although r_1 was held constant for the calculations, the geometric scaling of entire drawing does not change the field values. The magnetic permeability of the permanent magnetic material was also changed in each scenario. The relative permeability in the x and y axis, $\mu_{r,x}$ and $\mu_{r,y}$, ranged from 0.9 to 5. In one situation both values changed from 0.9 to 1.5 in steps of 0.1 and in a second situation they ranged from 1 to 5 in steps of 0.5. The remanent magnetization (B_r) was also changed from 0.5 to 2 T. Both the relative permeability and remanent magnetization ranges were chosen in such a way to cover most of the magnetic materials commercially available, as shown in Table 1.

In the FEMM simulator the remanent magnetization of the materials was defined by inserting the corresponding coercivity, H_C. It was assumed that B_r and H_C were linearly related by the equation $B_r = \mu H_C$. Since rotating the magnetization in the *xy* plane does not change the magnetic field strength or homogeneity (i.e. this is equivalent to rotating the magnet) 2D analyses do not include orthogonality and/or parallelism problems which could arise in a 3D analysis, such as having the magnetization tilted out of the *xy* plane.

All results were analyzed with the software Origin from OriginLab® [13]. Fitting curves were evaluated in their accuracy by looking at the coefficient of determination, R^2 [14].

3. Influence of the permanent magnet permeability

In the first analysis that was made, $\mu_{r,x}$ and $\mu_{r,y}$ were varied independently from 0.9 to 1.5 in steps of 0.1 in order to determine B_0 in the central point of the air gap of the magnet. These initial intervals were chosen as the relative permeabilities of most NdFeB magnets are situated in that range.

Eq. (1), through which the magnetic field in ideal HCM magnets can be calculated was first obtained by Peng et al. [9] Thus, it is known that when approaching ideal conditions, in which the permanent magnet is isotropic and $\mu_r = 1$, the magnetic field strength, B_0, must be dependent only on the thickness of the permanent magnet and its remanent magnetization, B_r, (Fig. 2).

$$B_0 = \frac{B_r}{2} \times \left[1 - \left(\frac{r_1}{r_2}\right)^2\right] \tag{1}$$

However, this equation gives us little information when dealing with real magnetic materials, which are not isotropic and $\mu_r \neq 1$.

Table 1
Data of commercially available materials as retrieved from Eclipse Magnetics datasheets (Chinese standards).

	B_r(T)	H_c(kA/m)	μ_r
NdFeB	1.03–1.43	793–1035	1.01–1.43
Ferrite	0.20–0.46	125–354	0.97–2.36
SmCo	0.30–1.15	199–845	0.78–1.77
AlNiCo	0.31–1.35	38–150	3.12–19.89

For this reason, we set out to find how the magnetic permeability affects the magnetic field in the central air gap region. From the above equation we know in advance that as the ratio r_2/r_1 grows to infinity, the magnetic field will reach a limit equal to $B_r/2$.

Thus, the first step in determining the effect of the relative permeability in the intensity of B_0 was to find how the upper limit, $B_r/2$, of Eq. (1) is affected by the relative permeabilities, knowing that when they are equal to 1, the limit $B_r/2$ must be obtained. For this reason, initially, r_2/r_1 was set to 10, since from this point on it can considered that B_0 has reached its maximum intensity, and either $\mu_{r,x}$ or $\mu_{r,y}$ set to 1. It was found for these cases that when relative permeability of each one of the axis is higher than 1 then the maximum magnetic field at the central air gap region is decreased. The dependency of B_0 with each of the permeabilities has a logarithm behavior (Eqs. (2) and (3)). All the fitting curves had an R^2 equal to 1.

$$B_0(\mu_{r,x}) = B_r\left[\frac{1}{2} - 0.125\ln\mu_{r,x}\right] \tag{2}$$

$$B_0(\mu_{r,y}) = B_r\left[\frac{1}{2} - 0.122\ln\mu_{r,y}\right] \tag{3}$$

Next it was necessary to find what effect the ratio r_2/r_1 would have on Eqs. (2) and (3). In this step of the computations r_2/r_1 was changed from 1.5 to 10 while also changing either $\mu_{r,x}$ or $\mu_{r,y}$ from 0.9 to 1.5 while the other was maintained equal to 1. Since both equations must be obtained when $r_2/r_1 \to \infty$, it was assumed that the resulting term to be added to both equations must have the form:

$$\chi(\mu_{r,i})(|\mu_{r,i} - 1|)\exp\left(-\frac{r_2}{r_1}\right) \qquad i = x, y \tag{4}$$

where $\chi(\mu_{r,i})$ is a function of $\mu_{r,x}$ or $\mu_{r,y}$. The term $|\mu_{r,i} - 1|$ ensures that the dependency on $\mu_{r,x}$ or $\mu_{r,y}$ equals zero if the permeability equals 1 and the exponential term guarantees that Eqs. (2) and (3) are obtained when $r_2/r_1 \to \infty$. As it turns out the functions $\chi(\mu_{r,x})$ and $\chi(\mu_{r,y})$ are of logarithmic nature and so Eqs. (2) and (3) become Eqs. (5) and (6). The R^2 of the fitting curves was always higher than 0.997.

$$\begin{aligned} B_0\left(\mu_{r,x}, \frac{r_2}{r_1}\right) = {} & B_r\left[\frac{1}{2} - 0.125\ln\mu_{r,x}\right] \times \left[1 - \left(\frac{r_1}{r_2}\right)^2\right] \\ & - \left[0.012 - 0.008\ln\left(\mu_{r,x} - 1\right)\right] \times \left|\mu_{r,x} - 1\right| \\ & \times \exp\left(-0.283\frac{r_2}{r_1}\right) \end{aligned} \tag{5}$$

$$\begin{aligned} B_0\left(\mu_{r,y}, \frac{r_2}{r_1}\right) = {} & B_r\left[\frac{1}{2} - 0.122\ln\mu_{r,y}\right] \times \left[1 - \left(\frac{r_1}{r_2}\right)^2\right] \\ & - \left[0.009 - 0.02\ln\left(\mu_{r,y} - 1\right)\right] \times \left|\mu_{r,y} - 1\right| \\ & \times \exp\left(-0.283\frac{r_2}{r_1}\right) \end{aligned} \tag{6}$$

So far only equations linking two of the three variables, either r_2/r_1 and $\mu_{r,x}$ or r_2/r_1 and $\mu_{r,y}$ had been found, since one of the relative permeability was always set to 1. After analyzing the data from the scenarios in which all three variables ($r_2/r_1, \mu_{r,x}, \mu_{r,y}$) were changed at once, a cross term which accounts for the combined influence of these three parameters had to be included in the equation. This term should approach 0 either when $r_2/r_1 \to \infty$, or when $\mu_{r,x} = 1$ or when $\mu_{r,y} = 1$. Therefore, it should have the form:

$$\varsigma(\mu_{r,x}, \mu_{r,y})(|\mu_{r,x} - 1|)(|\mu_{r,y} - 1|)\exp\left(-\frac{r_2}{r_1}\right) \tag{7}$$

where $\varsigma(\mu_{r,x}, \mu_{r,y})$ is a function of $\mu_{r,x}$ and $\mu_{r,y}$. It was found that function ς possessed an exponential decay term, dependent on both $\mu_{r,x}$ and $\mu_{r,y}$, as well as the sum of two negative logarithmic terms, dependent on $\mu_{r,i} - 1$, which finally yielded the equation of the magnetic field in the central air gap region, Eq. (8). The R^2 of the fitting curves was always greater than 0.9994.

$$B_0\left(\mu_{r,x}, \mu_{r,y}, \frac{r_2}{r_1}\right) = B_r\left[\frac{1}{2} - 0.125\ln\mu_{r,x} - 0.122\ln\mu_{r,y}\right] \times \left[1 - \left(\frac{r_1}{r_2}\right)^2\right] - \left\{\left[0.012 - 0.008\ln\left(\mu_{r,x} - 1\right)\right] \times \left(\mu_{r,x} - 1\right) + \left[0.09 - 0.02\ln\left(\mu_{r,y} - 0.88\right)\right] \times \left(\mu_{r,y} - 1\right)\right\} \times \exp\left(-0.283\frac{r_2}{r_1}\right) + \left[-7.83\exp\left(-1.32\mu_{r,x}\mu_{r,y}\right) - \frac{0.65}{\mu_{r,y}}\ln\left(\mu_{r,x} - 1\right) - \frac{0.49}{\mu_{r,x}}\ln\left(\mu_{r,y} - 1\right)\right] \times \left(\mu_{r,x} - 1\right)\left(\mu_{r,y} - 1\right)\exp\left(-0.21\frac{r_2}{r_1}\right) \quad (8)$$

It is important to note that while the logarithm term in function ς tends to infinity when $\mu_{r,i} = 1$ and the term $|\mu_{r,i} - 1|$ tends to zero at this point, there is no indetermination in the equation because: $\lim_{\mu_{r,i}\to 1} - \ln(\mu_{r,i} - 1) \times (\mu_{r,i} - 1) = 0$.

Eq. (8) can be safely used to determine the magnetic field in the bore of magnets whose relative magnetic permeability lies between 0.9 and 1.6 and the error of this equation in relation to the simulated value will not exceed 3.4%.

As can be seen in Fig. 3, the average difference between the magnetic field calculated from Eq. (8) and the values found through the simulations is on average below 1.5% and rises to 1.79% when r_2/r_1 is close to 1.5 and when $\mu_{r,x} - \mu_{r,y} = -0.5$. This shouldn't be a problem since the HCM magnets have an optimum r_2/r_1 ratio around 6, above which increasing the magnetic material does not significantly increase the magnetic field intensity. The average difference between the simulated magnetic field and Eq. (8) is less than 0.6% in most situations, but starts rising as r_2/r_1 comes closer to 1.5, and the difference $\mu_{r,x} - \mu_{r,y}$ closer to −0.5. This difference comes to its biggest value when $\mu_{r,x} - \mu_{r,y} = -0.5$, but nevertheless does not exceed 3.5%. A hypothesis for this is that after each curve fit the constants determined by the fitting software were rounded to 3 decimal places, this could be a source of propagated errors which could affect the result of the equation,

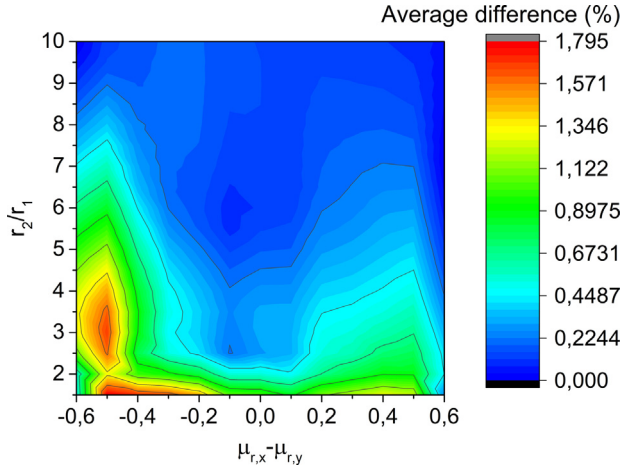

Fig. 3. Difference, in percentage, between the magnetic field intensity calculated from Eq. (8) and the magnetic field intensity found through simulation. The *x* axis shows $\mu_{r,x} - \mu_{r,y}$ and the *y* axis shows r_2/r_1.

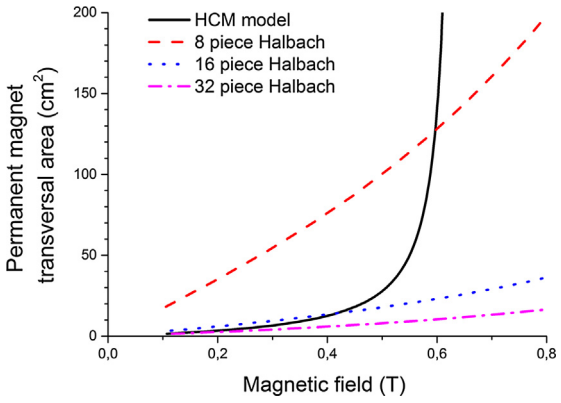

Fig. 4. Comparison between several Halbach array magnets and the HCM model where the magnetic material area needed (in a 2D simulation) is plotted against the maximum magnetic field output. The HCM B_r was considered to be 1.23 T and the magnetic material was isotropic, with $\mu_r = 1$. The internal air gap of all magnets had a radius of 15 mm and the Halbach magnets were simulated in such a way that the homogeneity was better than 10 ppm within a 10 mm radius in the air gap, as calculated through the equations presented in [7].

when compared to the simulation, at the limits of its operation. At the optimum ratio ($r_2/r_1 = 6$) the average difference between simulation and the equation will be lower than 1.4%.

By comparison, it was shown by Halbach in 1980 [15] that the magnetic field strength of the ideal Halbach array is given by $B_0 = B_r \cdot \ln\left(\frac{r_{outer}}{r_{inner}}\right)$. Although the real Halbach is segmented (which changes the way the magnetic field is related to the thickness of the material by introducing segmentation effects) the theoretical limit of the magnetic field is infinity, as it increases with the magnet thickness. Fig. 4 shows that for low magnetic field applications the HCM model requires less magnetic material to achieve a given field than a Halbach array of 16 pieces. Compared to a 32 piece Halbach array the amount of magnetic material is nearly the same (for low field applications) but taking into account that working with 32 magnetic pieces is much more challenging, it is possible to see the advantage of working with the HCM model. The HCM magnet is, however, limited when working with higher magnetic field intensities, since, as mentioned before, the magnetic field has an upper limit of $B_r/2$.

The second analysis extended the range of variation of $\mu_{r,x}$ and $\mu_{r,y}$ to 0.9 to 5 to include many other commercially available magnetic materials. An equation was sought for the magnetic field in these situations. In this case, however, even though the limit of the magnetic field intensity is easily determined, the functions $\chi(\mu_{r,i})$ and $\varsigma(\mu_{r,x}, \mu_{r,y})$ become much more complex and the resulting equation would be less likely to be used by someone designing one of these magnets. Nevertheless, should anyone be interested in designing a magnet using materials with relative permeabilities larger than 1.5 and lower than 1, the maximum magnetic field which can be obtained in the limit of a perfectly isotropic material and very large r_2/r_1 ratio ($r_2/r_1 \geqslant 9$) can be safely determined using the first line of Eq. (8):

$$B_0\left(\mu_{r,x}, \mu_{r,y}, \frac{r_2}{r_1}\right) = B_r\left[\frac{1}{2} - 0.125\ln\mu_{r,x} - 0.122\ln\mu_{r,y}\right] \times \left[1 - \left(\frac{r_1}{r_2}\right)^2\right] \quad (9)$$

4. Homogeneity

An important feature of magnets, especially those used for nuclear magnetic resonance purposes, is the magnetic field homogeneity. The homogeneity of the HCM magnet was evaluated when

the relative permeability changed from 0.9 to 5 in circular regions in the air varying from $0.1r_1$ to $0.9r_1$.

Homogeneity (H) was defined here, in ppm, as the average absolute deviation between the magnetic field at n points (B_i) within the central air gap region and the magnetic field intensity at the center of the magnet (B_0), as shown by the following equation:

$$H = \frac{1}{n}\frac{\sum_{i=1}^{n}|B_i - B_0|}{B_0 \times 10^{-6}} \tag{10}$$

Previous studies by Peng et al. showed that in ideal conditions this type of magnets produces a perfectly homogeneous magnetic field. Simulations with a precision of 10^{-10} showed that these magnets produce a quasi perfect homogeneous magnetic field (homogeneity below 0.075 ppm) as long as $\mu_{r,x}$ and $\mu_{r,y}$ are equal (Fig. 5a and e), regardless of the value. The homogeneity worsens as the difference $|\mu_{r,x} - \mu_{r,y}|$ becomes larger (Figs. 5a and b and 5c and d) and as the ratio r_2/r_1 becomes smaller (Fig. 5b, c and f). Furthermore, we found that the homogeneity within the air bore varies exponentially with r_2/r_1 (Fig. 6).

The three parameters, y_0, A and C_1 of the homogeneity exponential decay, $H = y_0 + A_1 \times \exp(-1/C_1 \times r_2/r_1)$, are dependent on the radius of the region on which the homogeneity is being calculated, ρ, given in fractions of r_1. Through curve fitting we found that parameters y_0 and A are proportional to the second power of ρ, while C_1 remains constant (all fitting curves had an R^2 bigger than 0.99999). The final equation of the homogeneity as a function of both r_2/r_1 and ρ is given by:

$$H = A \cdot \rho^2 + B \cdot \rho^2 \cdot \exp\left(-\frac{1}{C}\cdot\frac{r_2}{r_1}\right) \tag{11}$$

The parameters A, B and C are dependent on $\mu_{r,x}$ and $\mu_{r,y}$. An equation for parameters A, B and C was sought but could not be found. However, for a magnet designer it should be possible to

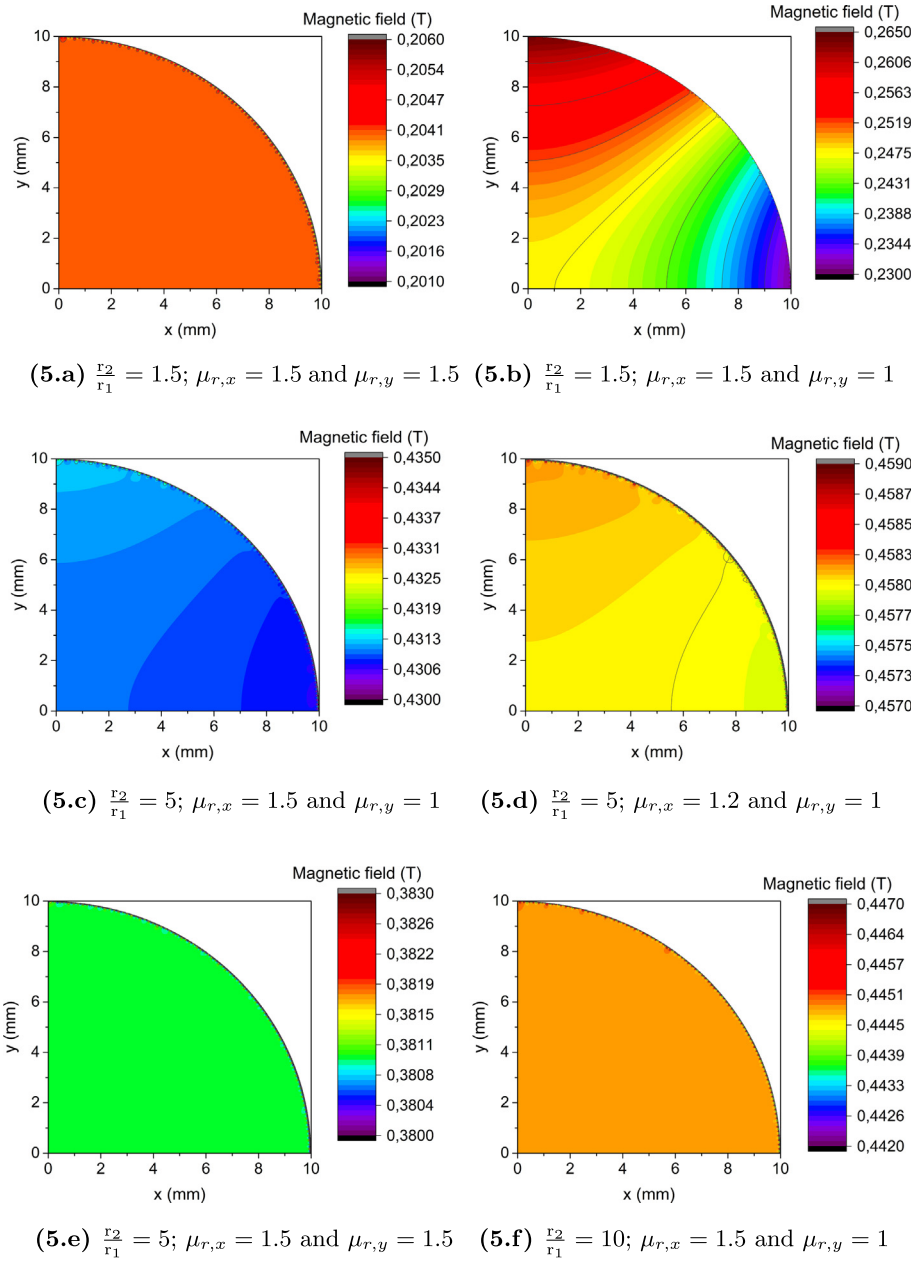

(5.a) $\frac{r_2}{r_1} = 1.5$; $\mu_{r,x} = 1.5$ and $\mu_{r,y} = 1.5$ **(5.b)** $\frac{r_2}{r_1} = 1.5$; $\mu_{r,x} = 1.5$ and $\mu_{r,y} = 1$

(5.c) $\frac{r_2}{r_1} = 5$; $\mu_{r,x} = 1.5$ and $\mu_{r,y} = 1$ **(5.d)** $\frac{r_2}{r_1} = 5$; $\mu_{r,x} = 1.2$ and $\mu_{r,y} = 1$

(5.e) $\frac{r_2}{r_1} = 5$; $\mu_{r,x} = 1.5$ and $\mu_{r,y} = 1.5$ **(5.f)** $\frac{r_2}{r_1} = 10$; $\mu_{r,x} = 1.5$ and $\mu_{r,y} = 1$

Fig. 5. Magnetic field distribution in different simulated scenarios.

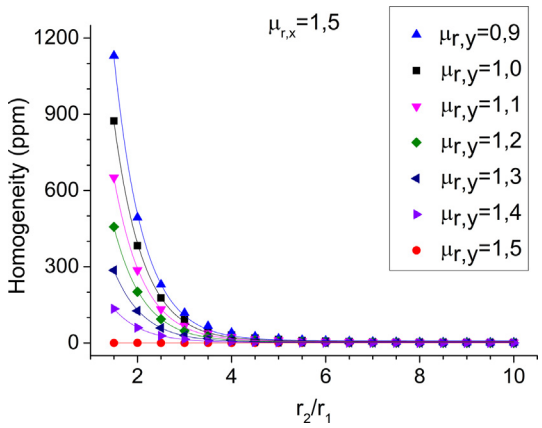

Fig. 6. Example graph of the homogeneity within the air gap of an HCM magnet with $r_1 = 10$ mm, calculated at the inner radius of 5 mm. $\mu_{r,x}$ was 1.5 and R^2 of all fitting curves was higher than 0.9991.

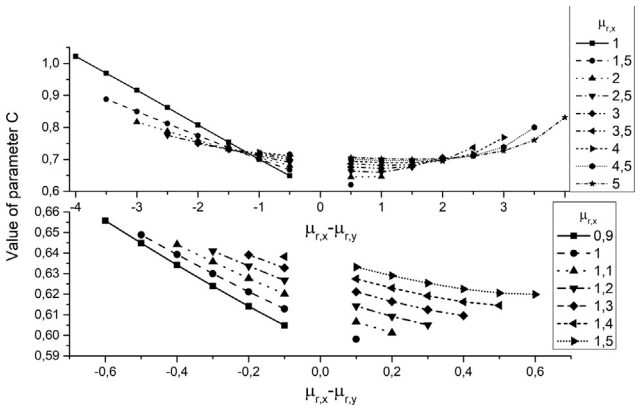

Fig. 9. Parameter C to be used in Eq. (11). Each line type and symbol represents one fixed value of $\mu_{r,x}$. $\mu_{r,y}$ can be calculated by using the x axis which shows the difference $\mu_{r,x} - \mu_{r,y}$.

determine the homogeneity in a certain region of the magnet by analyzing Figs. 7–9, which show the various parameters on the different cases. These graphs were plotted from the data of the computational simulations.

To find the homogeneity of an HCM magnet one must determine the values of parameters A, B and C from Figs. 7–9 by finding the line which represents the desired $\mu_{r,x}$. The relative permeability, $\mu_{r,y}$, can be determined by looking at the x axis, which shows $\mu_{r,x} - \mu_{r,y}$. The values of the three parameters must be input in Eq. (11) to find the homogeneity of the magnet.

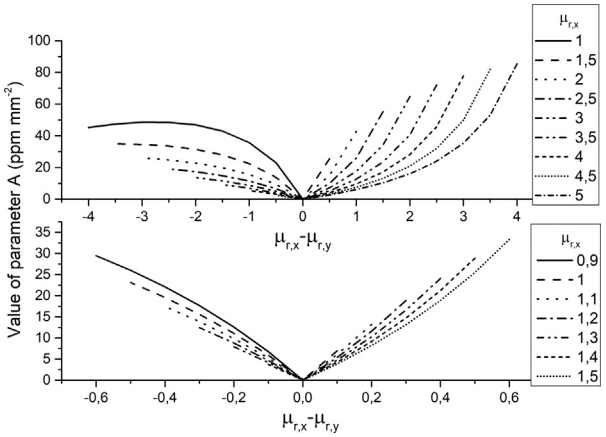

Fig. 7. Parameter A to be used in Eq. (11). Each line type represents one fixed value of $\mu_{r,x}$. $\mu_{r,y}$ can be calculated by using the x axis which shows the difference $\mu_{r,x} - \mu_{r,y}$.

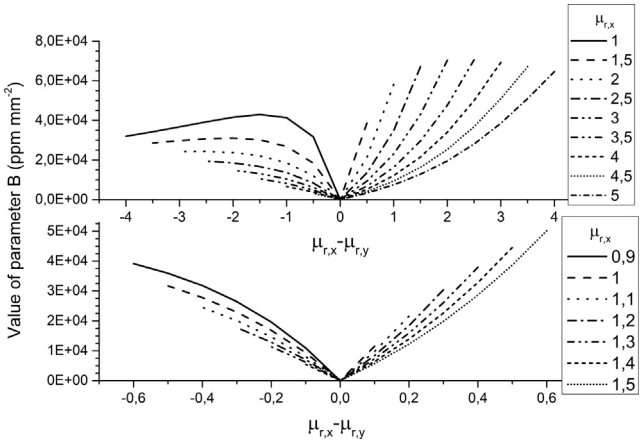

Fig. 8. Parameter B to be used in Eq. (11). Each line type represents one fixed value of $\mu_{r,x}$. $\mu_{r,y}$ can be calculated by using the x axis which shows the difference $\mu_{r,x} - \mu_{r,y}$.

As an example of the use of Eq. (11) together with the data in Figs. 7–9 consider the case of the HCM magnet presented in Fig. 5e, where $r_2 = 50$ mm, $r_1 = 10$ *mm* ($r_2/r_1 = 5$), $\mu_{r,x} = 1.5$ and $\mu_{r,y} = 1$. The magnet designer wants to find the homogeneity within a radius of 5 mm. In this case $\rho = 0.5$ and $\mu_{r,x} - \mu_{r,y} = 0.5$. Using this information we can find that parameter A equals approximately 25, parameter B is close to 38,000 and parameter C has the value of 0.62. Plugging all of this values in Eq. (11) we find that the homogeneity of this magnet will be of 9.4 ppm in the region of interest.

By comparison, the homogeneity of the magnetic field produced by a Halbach array is strongly dependent on the number of segments which constitute the array. Turek and Liszkowski showed that the homogeneity of the magnetic field increases as the number of segments increases and as the thickness of the PM increase [7].

Because the magnetic field that is generated by the HCM magnets is highly homogeneous when the permanent magnet is isotropic it is not necessary to build magnets with bores much bigger than the desired usable region. For measuring samples in 5 mm NMR tubes r_1 can be 5 mm and r_2 can be 30 mm. In the case of larger samples the ratio r_2/r_1 may be decreased so that the ordered magnets need not be too volumous, without great losses in magnetic field strength (r_2/r_1 = 5 or even 4).

5. Electromagnetic cylindrical configuration

It is possible to get a similar cylindrical configuration using electrical currents instead of a permanent magnet. In order to calculate how the spatial current distribution should be, it is assumed that the field $\mathbf{B}_0$ points in the y direction and is perfectly homogeneous in all the central air region. The integral Ampere's Law is applied in the closed curve C indicated in Fig. 10, according to Eq. (12):

$$\oint_C \frac{\mathbf{B}\cdot d\mathbf{l}}{\mu} = \oint_{C1} \frac{\mathbf{B}\cdot d\mathbf{l}}{\mu_0} + \oint_{C2} \frac{\mathbf{B}\cdot d\mathbf{l}}{\mu_0} + \oint_{C3} \frac{\mathbf{B}\cdot d\mathbf{l}}{\mu_f} = I_{enc} \tag{12}$$

where $\mathbf{B}$ is the magnetic field, $d\mathbf{l}$ is the infinitesimal element tangent to the curve C, μ is the magnetic permeability and I_{enc} is the current enclosed by the curve C.

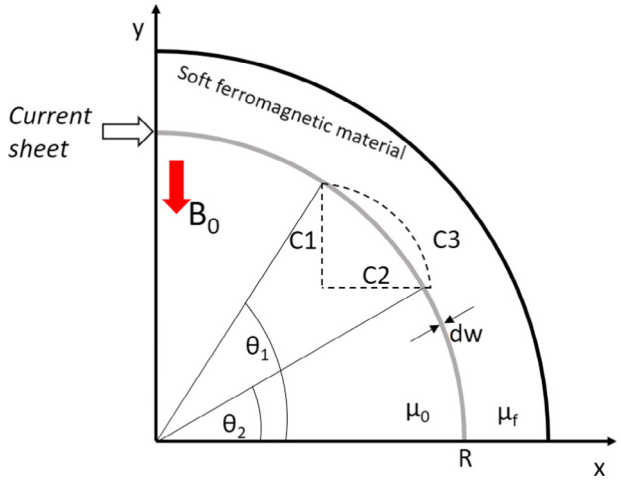

Fig. 10. First quadrant of the cylindrical configuration, where the symmetry conditions are being applied in the *x* axis ($\mathbf{B_0}$ is perpendicular) and *y* axis ($\mathbf{B_0}$ is parallel). The electrical current is coming out of the page. The thickness of the current sheet is dw.

As the soft ferromagnetic material of path C3 has its permeability much higher than the air ($\mu_f \gg \mu_0$), and its length is in the same order of C1 and C2, this integration can be neglected. The integration over C2 is null by the orthogonality between **B** and d**l** and Eq. (12) is reduced to:

$$\oint_{C1} \frac{\mathbf{B}\cdot d\mathbf{l}}{\mu_0} = \frac{B_0 R(\sin\theta_2 - \sin\theta_1)}{\mu_0} = I_{enc} \tag{13}$$

The current density K in a differential arc of length $Rd\theta$ can be determined making the difference $\theta_2 - \theta_1$ in Eq. (13) to tend to differential $d\theta$, yielding Eq. (14). This equation shows that K does not depend on R for the current sheet with thickness approaching zero (dw → 0):

$$K(\theta) = \frac{B_0 \cos\theta}{\mu_0} \tag{14}$$

Tests were made with the 2D FEMM magnetostatic simulator to check the validity of Eq. (14) – Fig. 11. The conductor was segmented in several small arcs and their currents calculated by (13).

In order to have an idea of the current densities for typical applications, a field of 0.2 T was created by coils with 10 turns per quadrant (9° per segment), with r_1 set to 50 mm. Using Eq. (13), the highest current is 1245 A in the segment from 0° to 9°. If the thickness of this current sheet is 5 mm, the current density is about 32 A mm^{-2}, which is too large for conventional conductors. However, such configuration should be favorable for superconducting coils in which current density is higher.

Even in the absence of the soft ferromagnetic external layer, the same current distribution creates a homogeneous field in the central air gap region - Fig. 12 - however, the intensity of the magnetic field in the absence of the ferromagnetic material will be decreased by 50%.

It was observed in the simulations that for very thin current sheets the field **B** is perpendicular to the circular trajectory in the mean radius of the current sheet (R_m), which means that the application of Ampere's Law over path C3 in Fig. 13 is null (see Appendix A).

For the same current distribution as the one given by Eq. (14) the application of Ampere's Law on the closed path C1-C2-C3 is equal to Eq. (13), except that the enclosed current is half of I_{enc} (Eq. (15)).

$$\oint_{C1} \frac{\mathbf{B}\cdot d\mathbf{l}}{\mu_0} = \frac{B_b R_m(\sin\theta_2 - \sin\theta_1)}{\mu_0} = \frac{I_{enc}}{2} \tag{15}$$

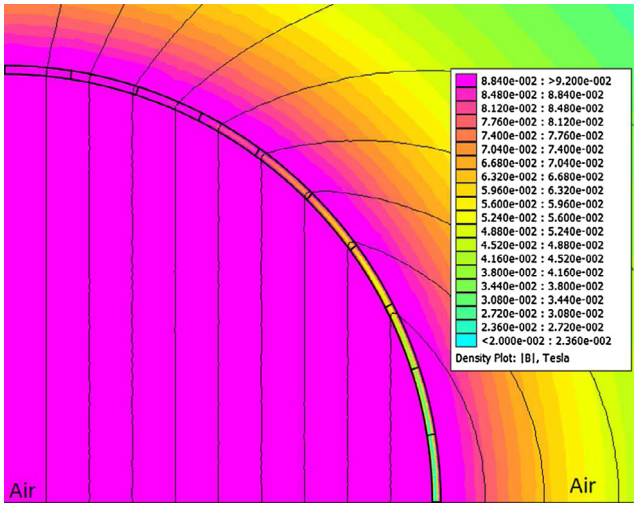

Fig. 12. Homogeneous field generated only by electrical currents.

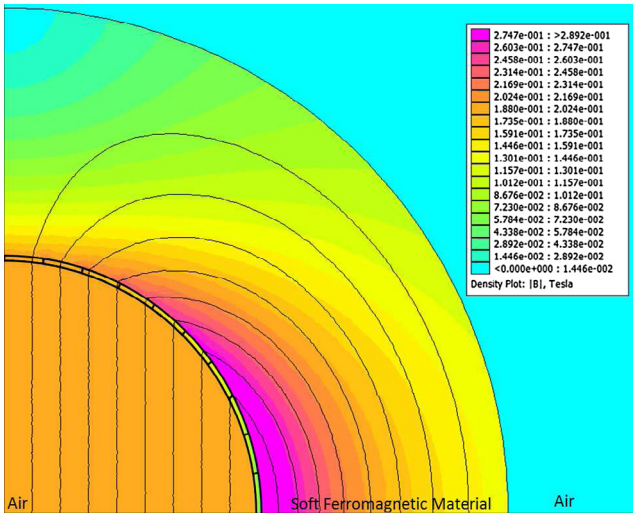

Fig. 11. 2D simulation of the electromagnetic cylindrical configuration. The electric conductor has been fragmented in 10 segments.

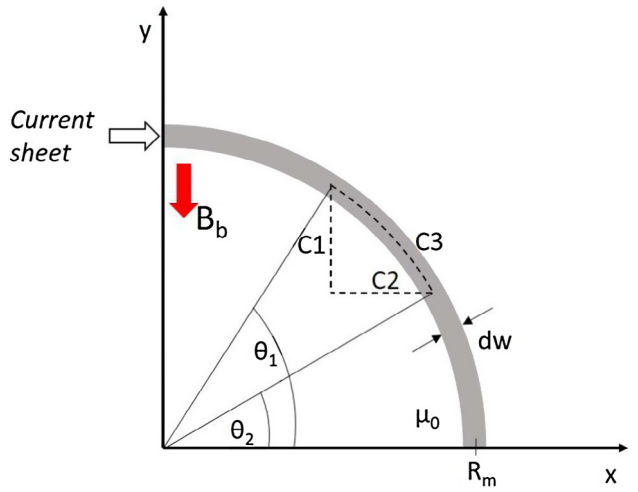

Fig. 13. Trajectory chosen for Ampere's Law in the cylindrical geometry only with the current sheet.

where B_b is the magnetic field intensity in the bore of the magnet.

Comparing Eqs. (13) and (15), considering the absence of the soft ferromagnetic external layer and assuming $R_m = R$, the magnetic field in the bore of the electromagnetic HCM magnet, B_b, is equal to $B_0/2$, oriented in the y direction.

This result was checked against simulation with $R_m \gg dw$ and taking a highly segmented current sheet and an analytical proof of this is found in Appendix B.

Using the results in Appendix B it is possible to determine the magnetic field in the bore of a permanent magnet cylinder which is not enclosed in a soft ferromagnetic material. This is done by replacing the permanent magnet by two current sheets, one in the inner radius of the magnet and the other on the external radius. The current density of each of the current sheets is given by:

$$K_{internal}(\theta) = \frac{B_0 \cos\theta}{\mu_0} \tag{16}$$

$$K_{external}(\theta) = -\frac{B_0 \cos\theta}{\mu_0} \tag{17}$$

The magnetic field generated in the bore by a current sheet with current density $K_i(\theta)$ is equal to $\frac{B_0}{2}\hat{e}_y$ and the magnetic field generated in the bore by a current sheet with current density $K_e(\theta)$ is equal to $-\frac{B_0}{2}\hat{e}_y$. Therefore the total magnetic field in the bore of the magnet is equal to zero. This result is in accord with the theory developed by Halbach in his 1980 paper [15]. The field outside the magnet is found by using the equations found in Appendix B.

This electromagnetic configuration could potentially be an alternative to current superconducting magnets. However, building this coil may pose some challenges, as the winding is not as simple as winding a wire around a tube, as is the case with solenoidal coils. Furthermore a precise control of the currents in each of the wires is critical in order to achieve a highly homogeneous magnetic field.

There are advantages to using the electromagnetic HCM. Generally, superconducting magnets are solenoidal coils, which generate an axial magnetic field. This requires that the excitation/receiver coil generates a magnetic field in the XY plane, which can be done by using saddle-shaped coils, for example. With the use of the electromagnetic HCM the possibility of using solenoidal coils as excitation/receiver coils is available. This could be advantageous since solenoids are much easier to build than other more complex coil geometries. In comparison to saddle-shaped coils, for example, solenoid coils have a signal-to-noise ratio that is three times as large as that of saddle-shaped coils, which is translated into 90° pulses which are three times shorter (with the same radio-frequency power) in solenoidal coils than in saddle-shaped coils [16]. Another advantage may be that if the magnet is built with the high permeability external layer the magnetic field may be doubled (or lower currents can be used) and in addition the magnet will be naturally shielded, which reduces security issues in the laboratory.

6. Conclusions

From these studies it is possible to conclude that the HCM magnets, whether electromagnetic or using permanent magnets, should produce a highly homogeneous magnetic field (below 0.075 ppm in simulations), which is useful for applications where high magnetic homogeneity is important, as is the case with NMR. In the case of anisotropic magnetic materials the homogeneity of the magnetic field in different regions of the bore can be determined using Eq. (11) and the data of Figs. 7–9. The magnetic field intensity can be determined through Eq. (8) when the relative permeability of the material lies between 1 and 1.6. For materials whose relative permeability is outside this region only the maximum magnetic field output in ideal conditions (isotropic material and $r_2/r_1 \geqslant 9$) can be determined.

Because the magnetic field that is generated is highly homogeneous when the permanent magnet is isotropic it is not necessary to build magnets with bores much bigger than the desired usable region. For measuring samples in 5 mm NMR tubes r_1 can be 5 mm and r_2 can be 30 mm. In the case of larger samples the ratio r_2/r_1 may be decreased so that the ordered magnets need not be too volumous, without great losses in magnetic field strength. It is worth pointing out that the information regarding magnetic permeability is usually given by the magnet manufacturers, through BH curves. On another practical note, one way to ensure that magnets have the specified characteristics for building the HCM magnet is to ask the manufacturer to guarantee that specifications are met, which can increase the cost of the permanent magnet or; to buy several magnets and, through trial and error, select the best one.

The electromagnetic HCM can potentially be used in high-field NMR superconducting spectrometers for generating the static B_0 field, since the generated B_0 should be more homogeneous than the one produced by a simple solenoid and does not require complex techniques to improve its homogeneity (as is the case with solenoidal coils).

While the topic that has been studied has, by no means, been fully explored, especially because other problems that may be encountered while building these magnets have not been analysed (non-homogeneous magnetization of the permanent magnets and further investigations on the electromagnetic HCM) it is believed that this study may serve to increase the interest in HCM magnets enough to justify exploring all the other challenges surrounding this configuration.

Acknowledgments

Funding: This work was supported by the Brazilian funding agencies CNPq and FAPESP. CNPq grants number 161555/2015-2 and 140989/2015-3 and FAPESP grants number 2014/22126-9 and 2017/12864-0.

Appendix A. Magnetic field orientation in the mean radius of the current sheet

To calculate the magnetic field orientation in the mean radius of the current sheet first consider a pair of concentric cylindrical conductors, I and II, with the same current density (given by (14)), as shown in Fig. A.14. Conductors I and II are placed at $R_m - d$ and $R_m + d$, respectively. They are separated by a distance $2d$ and are symmetrical in relationship to $r = R_m$.

From Eq. (B.17), we find that the total magnetic field at $r = R_m$ is:

$$\underline{B}_T^*(R_m, \phi) = i\frac{B_0}{2} - i\frac{B_0 e^{-i2\phi}(R_m - d)^2}{2R_m^2} \tag{A.1}$$

If $R_m \gg d$:

$$\underline{B}_T^*(R_m, \phi) = i\frac{B_0}{2}(1 - e^{-i2\phi}) \tag{A.2}$$

Using Euler's equation, $e^{ix} = \cos x + i \sin x$, in Eq. (A.2) and going back to the vectorial notation $\mathbf{B} = B_x\hat{\mathbf{e}}_\mathbf{x} + B_y\hat{\mathbf{e}}_\mathbf{y}$:

$$\mathbf{B}_T = \frac{B_0}{2}\{-\sin(2\phi)\hat{\mathbf{e}}_\mathbf{x} + [\cos(2\phi) - 1]\hat{\mathbf{e}}_\mathbf{y}\} \tag{A.3}$$

If $\mathbf{v}_t = -\sin\phi\,\hat{\mathbf{e}}_\mathbf{x} + \cos\phi\,\hat{\mathbf{e}}_\mathbf{y}$ represents the unit vector tangent to the circumference at the point (R_m, ϕ), then:

$$\mathbf{B}_T \cdot \mathbf{v}_t = \frac{B_0}{2}\{\sin(2\phi)\sin\phi + [\cos(2\phi) - 1]cos\phi\} = 0 \tag{A.4}$$

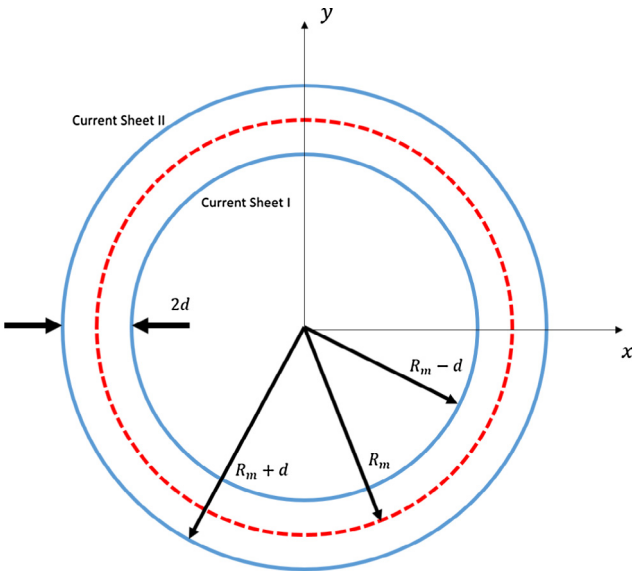

Fig. A.14. Geometry of a pair of conductors (blue lines) used to calculate the magnetic field orientation in the mean radius (red dashed line). (For interpretation of the references to colour in this figure legend, the reader is referred to the web version of this article.)

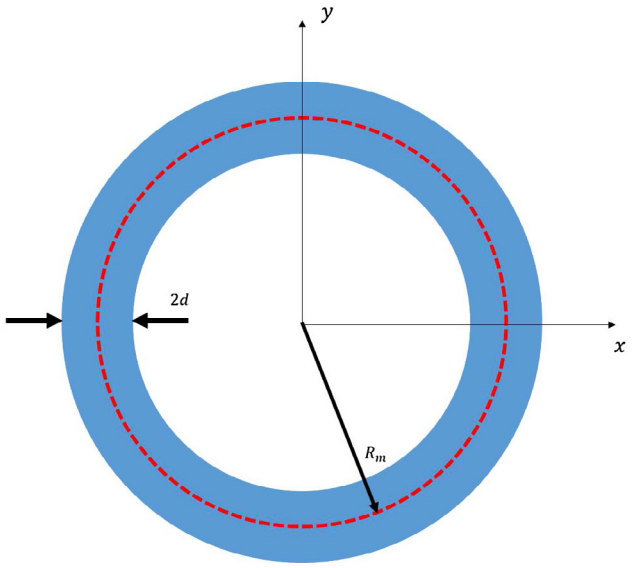

Fig. A.15. Illustration of a conductor of thickness $2d$ formed by piling several symmetric cylindrical conductors around the mean radius, R_m.

Eq. (A.4) shows that vector $\mathbf{B}_T$ is perpendicular to the circumference of radius R_m. If pairs of concentric cylindrical conductors are piled symmetrically around $r = R_m$ in such a way that a conductor of thickness $2d$ is formed (see Fig. A.15), then the magnetic field of this conductor will be perpendicular to the circumference at $r = R_m$, as long as $R_m \gg d$. Therefore, the integration over path C3 in Fig. 13 is null.

Appendix B. Magnetic field generated by electromagnetic HCM (without ferromagnetic material)

The magnetic field generated in the bore of an electromagnetic HCM without a surrounding soft ferromagnetic material can be calculated in the following way.

Considering the configuration of Fig. 13 for a current sheet with thickness approaching zero ($dw \to 0$) and linear current density given by Eq. (14). The differential current, dI is given by:

$$dI = K(\theta)dl = K(\theta)Rd\theta = \frac{B_0 R\cos\theta}{\mu_0}d\theta \tag{B.1}$$

Switching to a complex notation, the two-dimensional **B** field is given by $\underline{B} = B_x + iB_y$ and $\underline{B}^*$ is the complex conjugate of $\underline{B}$ [15]. Using this notation we have the following equation for the field generated by a current filament dI:

$$d\underline{B}^*(\underline{z}_0) = \frac{\mu_0 dI}{2\pi i}\frac{1}{\underline{z}_0 - \underline{z}} \tag{B.2}$$

where $\underline{z}$ represents the region in space where the current elements are located and $\underline{z}_0$ is the point at which the magnetic field will be calculated. Substituting Eq. (B.1) in (B.2) and taking the integral on the closed path C which has radius R and with θ ranging from 0 to 2π:

$$\underline{B}^*(\underline{z}_0) = \oint_C \frac{B_0}{2\pi i}\frac{R\cos\theta}{\underline{z}_0 - \underline{z}}d\theta \tag{B.3}$$

Making the following definition: $\underline{z} = Re^{i\theta}$, from which we have:

$$d\theta = \frac{d\underline{z}}{i\underline{z}} \tag{B.4}$$

and

$$R\cos\theta = \frac{\underline{z} + \underline{z}^*}{2} \tag{B.5}$$

where $\underline{z}^*$ is the complex conjugate of $\underline{z}$. Substituting both of these equations in (B.3) and developing the following equation is obtained:

$$\underline{B}^* = \oint_C \frac{B_0}{4\pi}\left(1 + \frac{\underline{z}^*}{\underline{z}}\right)\left(\frac{1}{\underline{z} - \underline{z}_0}\right)d\underline{z} \tag{B.6}$$

From the property $zz^* = R^2$, we get $z^* = R^2/z$. Substituting this in Eq. (B.6):

$$\underline{B}^* = \frac{B_0}{4\pi}\left[\oint_C \frac{d\underline{z}}{\underline{z} - \underline{z}_0} + R^2\oint_C \frac{d\underline{z}}{\underline{z}^2(\underline{z} - \underline{z}_0)}\right] \tag{B.7}$$

Let f be an analytic and holomorphic function inside and along a closed loop L in the complex plane. Then for every $\underline{a}$ inside L:

$$\oint_L \frac{f(\underline{z})}{(\underline{z} - \underline{a})^{n+1}}d\underline{z} = \frac{2\pi i f^{(n)}(\underline{a})}{n!} \tag{B.8}$$

where $f^{(n)}$ is the n-th derivative of f and, by convention, the contour integral is taken in the counter-clockwise direction. Eq. (B.8) is known as Cauchy's Integral Formula [17], and is valid in the following conditions:

1. $\underline{a}$ is inside the closed loop L;
2. $f(\underline{z})$ is analytic inside L, that is to say that all the poles of $f(\underline{z})$ must lie outside L.

B.1. Solution for $|\underline{z}_0| < |\underline{z}|$

Using Cauchy's Formula on the first integral of Eq. (B.7) in the region $|\underline{z}_0| < |\underline{z}|$:

$$\oint_C \frac{d\underline{z}}{\underline{z} - \underline{z}_0}\bigg|_{|\underline{z}_0|<|\underline{z}|} = 2\pi i \tag{B.9}$$

Regarding the second integral, the function $1/[\underline{z}^2(\underline{z} - \underline{z}_0)]$ has a pole at the origin and at $\underline{z} = \underline{z}_0$, both inside contour C. According to the Cauchy-Goursat theorem [18], circulation around C may be split into the circulation of the same function around the pole at the origin (path C_1) added to the circulation around the pole at $\underline{z} = \underline{z}_0$ (path C_2). This splitting of the loop C (see Fig. B.16) guarantees that conditions 1 and 2 are satisfied.

$$\oint_C \frac{d\underline{z}}{\underline{z}^2(\underline{z}-\underline{z}_0)}\bigg|_{|\underline{z}_0|<|\underline{z}|} = \oint_{C_1} \frac{\left(\frac{1}{\underline{z}-\underline{z}_0}\right)}{(\underline{z}-0)^2}d\underline{z} + \oint_{C_2} \frac{\left(\frac{1}{\underline{z}^2}\right)}{\underline{z}-\underline{z}_0}d\underline{z} \tag{B.10}$$

Applying Cauchy's Integral Formula:

$$\oint_C \frac{d\underline{z}}{\underline{z}^2(\underline{z}-\underline{z}_0)}\bigg|_{|\underline{z}_0|<|\underline{z}|} = 2\pi i \frac{d}{d\underline{z}}\left(\frac{1}{\underline{z}-\underline{z}_0}\right)\bigg|_{\underline{z}=0} + 2\pi i\left(\frac{1}{\underline{z}^2}\right)\bigg|_{\underline{z}=\underline{z}_0} = -\frac{2\pi i}{\underline{z}_0^2} + \frac{2\pi i}{\underline{z}_0^2} = 0 \tag{B.11}$$

Therefore:

$$\underline{B}^*|_{|\underline{z}_0|<|\underline{z}|} = \frac{B_0}{4\pi}(2\pi i + 0) = i\frac{B_0}{2} \tag{B.12}$$

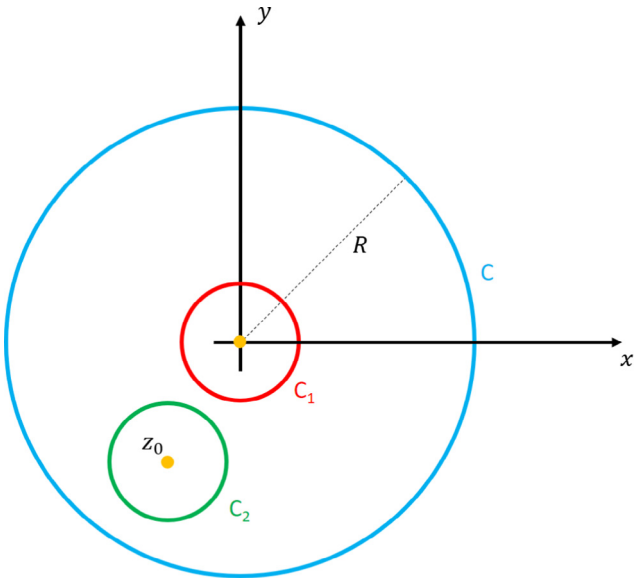

Fig. B.16. Illustration of the closed loops C (blue line), C_1 (red line) and C_2 (green line) in the complex plane. The origin and the point $\underline{z} = \underline{z}_0$ are the poles of the function $1/[\underline{z}^2(\underline{z}-\underline{z}_0)]$, and lie inside C. (For interpretation of the references to colour in this figure legend, the reader is referred to the web version of this article.)

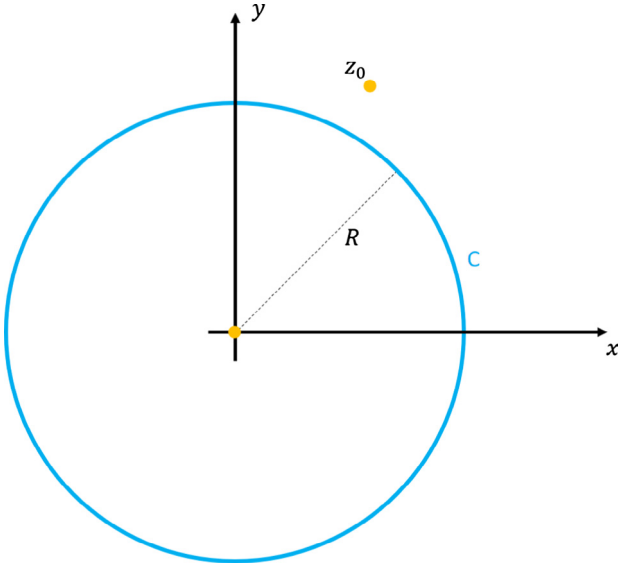

Fig. B.17. Illustration of the positioning of the poles at the origin and at $\underline{z} = \underline{z}_0$ in the complex plane. Since $|\underline{z}_0| > |\underline{z}|$, the point $\underline{z}_0$ lies outside the closed loop C.

B.2. Solution for $|\underline{z}_0| > |\underline{z}|$

Since $\underline{z}_0$ is outside C for $|\underline{z}_0| > |\underline{z}|$, the first integral of Eq. (B.7) is null.

$$\oint_C \frac{d\underline{z}}{\underline{z}-\underline{z}_0}\bigg|_{|\underline{z}_0|>|\underline{z}|} = 0 \tag{B.13}$$

For the second integral of Eq. (B.7), the pole at the origin lies inside C, while the pole at $\underline{z} = \underline{z}_0$ lies outside (Fig. B.17). Thus we have:

$$\oint_C \frac{d\underline{z}}{\underline{z}^2(\underline{z}-\underline{z}_0)}\bigg|_{|\underline{z}_0|>|\underline{z}|} = \oint_C \frac{\left(\frac{1}{\underline{z}-\underline{z}_0}\right)}{(\underline{z}-0)^2}d\underline{z} = -\frac{2\pi i}{\underline{z}_0^2} \tag{B.14}$$

Therefore:

$$\underline{B}^*|_{|\underline{z}_0|>|\underline{z}|} = \frac{B_0}{4\pi}\left(0 - \frac{2\pi i}{\underline{z}_0^2}\right) \tag{B.15}$$

Defining $\underline{z}_0 = re^{i\phi}$, we get:

$$\underline{B}^*|_{|\underline{z}_0|>|\underline{z}|} = -i\frac{B_0 e^{-i2\phi}R^2}{2r^2} \tag{B.16}$$

B.3. General solution of $\underline{B}^*$

By the following definitions, $|\underline{z}_0| = r$ e $|\underline{z}| = R$, and taking into account all that has been presented so far, the general solution of $\underline{B}^*$ can be written as:

$$\underline{B}^*(r,\phi) = \begin{cases} i\frac{B_0}{2}, & r < R \\ -i\frac{B_0 e^{-i2\phi}R^2}{2r^2}, & r > R \end{cases} \tag{B.17}$$

References

[1] L.A. Colnago, F.D. Andrade, A.A. Souza, R.B.V. Azeredo, A.A. Lima, L.M. Cerioni, T. M. Osán, D.J. Pusiol, Why is inline nmr rarely used as industrial sensor? Challenges and opportunities, Chem. Eng. Technol. 37 (2) (2014) 191–203.
[2] J. Mitchell, L. Gladden, T. Chandrasekera, E. Fordham, Low-field permanent magnets for industrial process and quality control, Prog. Nucl. Magnet. Reson. Spectrosc. 76 (2014) 1–60.
[3] B. Blümich, Introduction to compact nmr: a review of methods, TrAC Trends Anal. Chem. 83 (Part A) (2016) 2–11.
[4] O. Instruments, NMR spectrometers, 2017 <https://www.oxford-instruments.com/products/spectrometers/nuclear-magnetic-resonance-nmr>.
[5] Magritek, Magritek Homepage, 2017 <http://www.magritek.com/>.
[6] Nanalysis, Nanalysis Homepage, 2017 <http://www.nanalysis.com/>.
[7] K. Turek, P. Liszkowski, Magnetic field homogeneity perturbations in finite Halbach dipole magnets, J. Magnet. Reson. 238 (2013) 52–62.
[8] H. Soltner, P. Blümler, Dipolar Halbach magnet stacks made from identically shaped permanent magnets for magnetic resonance, Conc. Magnet. Reson. Part A 36 A (4) (2010) 211–222.
[9] Q. Peng, S.M. McMurry, J.M.D. Coey, Cylindrical permanent-magnet structures using images in an iron shield, IEEE Trans. Magnet. 39 (4) (2003) 1983–1989.
[10] P. Nath, C.K. Chandrana, D. Dunkerley, J.A. Neal, D. Platts, The "shim-a-ring" magnet: configurable static magnetic fields using a ring magnet with a concentric ferromagnetic shim, Appl. Phys. Lett. 102 (2013) 202409.
[11] P. Nath, K. Chandrana, Permanent magnet options for magnetic detection and separation - ring magnets with a concentric shim, US patent n° WO2012174148 A2 (June 13, 2012).
[12] D. Meeker, Finite Element Method Magnetics <http://www.femm.info/wiki/HomePage> (accessed 19 January 2016).
[13] Origin (Originlab, Northampton, MA).
[14] S.M. Ross, Introduction to Probability and Statistics for Engineers and Scientists, fifth ed., Academic Press, Boston, 2014.
[15] K. Halbach, Design of permanent multipole magnets with oriented rare earth cobalt material, Nucl. Instrum. Meth. 169 (1) (1980) 1–10.
[16] D. Hoult, R. Richards, The signal-to-noise ratio of the nuclear magnetic resonance experiment, J. Magnet. Reson. 24 (2) (1976) 71–85 (magnetic Moment).
[17] R.V. Churchill, J.W. Brown, Complex Variables and Applications, ninth ed., McGraw-Hill Education, New York, 2014.
[18] R.V. Churchill, J.W. Brown, Complex Variables and Applications, ninth ed., McGraw-Hill Education, New York, 2014.